01 Mar 2023

Anisotropic Thermal Expansion in High-Entropy Multicomponent Alb2-Type Diboride Solid Solutions

Frédéric Monteverde

Mattia Gaboardi

Federico Saraga

Lun Feng

et. al. For a complete list of authors, see https://scholarsmine.mst.edu/math_stat_facwork/1141

Recommended Citation

F. Monteverde et al., "Anisotropic Thermal Expansion in High-Entropy Multicomponent Alb2-Type Diboride Solid Solutions," *International Journal of Extreme Manufacturing*, vol. 5, no. 1, article no. 015505, Institute of Physics - IOP Publishing, Mar 2023.
The definitive version is available at https://doi.org/10.1088/2631-7990/acabee

OPEN ACCESS
IOP Publishing | IMMT
International Journal of Extreme Manufacturing
Int. J. Extrem. Manuf. **5** (2023) 015505 (13pp)
https://doi.org/10.1088/2631-7990/acabee

Anisotropic thermal expansion in high-entropy multicomponent AlB_2-type diboride solid solutions

Frédéric Monteverde[1,*], Mattia Gaboardi[2], Federico Saraga[1,4], Lun Feng[3,5], William Fahrenholtz[3] and Gregory Hilmas[3]

[1] National Research Council of Italy, Institute of Science Technology and Sustainability for Ceramics, Faenza 48018, RA, Italy
[2] Elettra—Sincrotrone Trieste S.C.P.A, Strada Statale 14—Km 163, 5 in AREA Science Park, Basovizza 34149, Trieste, Italy
[3] Missouri University of Science and Technology, Rolla, MO 65409, United States of America

E-mail: frederictullio.monteverde@cnr.it

Received 26 May 2022, revised 7 September 2022
Accepted for publication 15 December 2022
Published 29 December 2022

Abstract

High-entropy (HE) ultra-high temperature ceramics have the chance to pave the way for future applications propelling technology advantages in the fields of energy conversion and extreme environmental shielding. Among others, HE diborides stand out owing to their intrinsic anisotropic layered structure and ability to withstand ultra-high temperatures. Herein, we employed *in-situ* high-resolution synchrotron diffraction over a plethora of multicomponent compositions, with four to seven transition metals, with the intent of understanding the thermal lattice expansion following different composition or synthesis process. As a result, we were able to control the average thermal expansion (TE) from 1.3×10^{-6} to 6.9×10^{-6} K^{-1} depending on the combination of metals, with a variation of in-plane to out-of-plane TE ratio ranging from 1.5 to 2.8.

Supplementary material for this article is available online

Keywords: ultra-high temperature ceramics, borides, high-entropy ceramics, spark plasma sintering, synchrotron diffraction, anisotropic thermal expansion

1. Introduction

Disordered multi-component metal alloys were proposed in 2004 as innovative materials with promising applications [1]. The motivation was to stabilize (near)-equimolar mixtures and maximize the configurational entropy of mixing (ΔS_{MIX}) to increase the thermodynamic stability of the systems [2]. These compositions became known as high-entropy (HE) materials and occupy some of the least studied regions of phase diagrams. In 2015, entropy stabilization was demonstrated for the first time for a system of oxide compounds [3]. In the panorama of other compounds, HE disordered systems with improved properties were rapidly developed by exploring the addition of phases to obtain materials with a desirable blend of properties [4].

Ultra-high temperature ceramics (UHTCs) are a class of high performance materials that have melting temperatures

[4] Now working at AUREL Spa, I-47 015 (Modigliana, Italy).
[5] Now working at BLUE ORIGIN, 98 302 (Kent, Washington US).
[*] Author to whom any correspondence should be addressed.

above 3300 K. UHTCs consist of a limited number of early transition metal diborides, carbides, and nitrides, such as HfB_2, ZrB_2, HfN, and TaC [5]. UHTCs are useful in wide-ranging technologies due to the ability to withstand extreme environments that are beyond the capabilities of existing structural materials. Some of the extreme environments of interest include neutron irradiation shielding for the new generations of fusion/fission reactors and thermal protection systems for hypersonic aerospace vehicles.

HE-UHTCs are proposed for use at elevated temperatures where entropy dominates the free-energy landscape [5]. As such, new HE-UHTCs have been developed that are based on diborides and carbides that contain five or more transition metals of the groups IV, V, or VI in a single crystalline phase with random metal site occupancy. The plethora of possible combinations makes the discovery of ad hoc disordered materials an area extremely rich of opportunities. In applications such as environmental barrier coatings, differences in thermal expansion (TE) between an external ceramic coating and metallic substrate are a technological barrier when the TE mismatch diverges significantly at high temperatures. HE ceramics may offer a solution to this problem, using the composition-by-design as a tool for the tuning of TE to match specific requirements. To this end, HE ceramics could enable environmental thermal barrier coatings (E-TBCs) with operating temperatures exceeding 1400 K that have both lower thermal conductivity and adjustable TE values for the next-generation high-efficiency and thrust-weight ratios turbine engines [6–13]. Not surprisingly, the TE behaviour of HE oxides [10–13] has been investigated more extensively than HE diborides or carbides since successful syntheses of single phase oxides and subsequent TE measurements require less stringent experimental set-ups. Understanding the TE behaviour requires also considering the anisotropic character that can induce uneven strains at the E-TBC/substrate interface. However, few studies have been dedicated to this topic [6, 12].

TE investigations of non-oxide HE ceramics like borides [14–17] or carbides [18–20] have been limited and most studies have only speculated about the effects. Computational studies suggest that the compositional diversity may affect TE [15, 20]. However, experimental studies of the TE of HE borides and carbides remain sparse at best [15–17]. Iwan *et al* investigated the equation of state of $(Hf,Nb,Ta,Ti,Zr)B_2$ up to 2000 K[14] and found a non-linear volumetric thermal expansion with coefficients $\alpha_0 = -1.1 \times 10^{-5}$ K^{-1}, $\alpha_1 = 3.4 \times 10^{-8}$ K^{-2} and $\alpha_2 = 2.97$ K at 7.6 GPa. Dai *et al* predicted the temperature dependence of the Hf–Nb–Ta–Ti–Zr–B system using molecular dynamics (MD) [15]. However, a recent experimental analysis of single-phase $(Hf,Nb,Ta,Ti,Zr)B_2$ from 300 K to 1273 K showed a different behaviour, with an anisotropic trend with temperature [16]. In fact, the calculated cell parameters at 298 K for an ideally modelled nearly equimolar $(Hf,Nb,Ta,Ti,Zr)B_2$ solid solution did not differ significantly from those refined in the as-synthesized sample [16]. However, the experimental temperature dependent lattice evolution appeared to be remarkably different from the ideal model, showing an opposite trend of the TE coefficient along the basal and the prismatic direction. As a result, the average expansion did not change excessively compared to what was simulated for the ideal case, while the TE anisotropy assumed a steeper negative slope.

To gain a deeper understanding about TE behaviour in HE diborides and to demonstrate that the behaviour that was found in [16] for $(Hf,Nb,Ta,Ti,Zr)B_2$ was not an isolated case, it was carried out an extended study on a large collection of AlB_2-type multi-component diboride solid solutions (DSSs). A group of 20 different compositions was synthesized, with Ti and Zr as common metals among all compositions (see table 1) and containing 4, 5, 6, or 7 metals. Of these, 6 were obtained by selectively replacing Nb in $(Hf,Nb,Ta,Ti,Zr)B_2$ (C11 in table 1) with Cr, Mo, W, or V (i.e. C-5 and from C-11 to C-15). Another 3 compositions were obtained by enhancing the chemical complexity of C-11 by adding up to seven different transition metals (i.e. samples from C-19 to C-21). Furthermore, to study the effect of Nb concentration in C-11, additional 3 compositions were synthesized with different concentrations (i.e. samples from C-8 to C-10). Finally, the remaining 9 compositions differ from C-11 for a replacement of Hf and/or Ta with Nb, Mo, or W (i.e. samples from C-1 to C-4, C-6, C-7, and from C-16 to C-18). Composition C-5 and C-13 have the same metals sequence but were subjected to a different processing history. This ensemble was selected based on the idea of engineering the TE behaviour by tuning the chemical complexity of a starting composition. The compositional complexity induced by the coexistence of chemical species with differing characteristics leads to have solid solutions with non-ideal mixing behaviour. One of the effects induced by the just mentioned non-ideality is the local charge redistribution (i.e. differential local electronegativity (EN)) which can lead to tuneable properties that cannot be reliably predicted from the rule-of-mixture (RoM) [15].

With the support of synchrotron radiation x-ray powder diffraction (SR-XRPD), the TE trend for a wide panel of different HE DSSs was experimentally measured and critically analysed.

2. Experimental

Commercially available powders were used to prepare the single-phase multicomponent DSSs. The syntheses were accomplished through boro-carbothermal reduction reactions, adding boron carbide (B_4C, purity 96.8%, ~0.8 μm, H.C. Starck) and carbon black (C, BP120, 30 m^2 g^{-1}, Cabot) as reducing agents for the designed metal (Me) oxide mixtures. The following oxides were used: hafnium oxide (HfO_2, 99%, −325 mesh; Alfa Aesar), zirconium oxide (ZrO_2, 99%, SC101, mean size 0.8 μm, MEL Chemicals), titanium oxide (TiO_2, 99.9%, P25, mean size 20 nm, Degussa), tantalum oxide (Ta_2O_5, 99.85%, −325 mesh, Alfa Aesar), niobium oxide (Nb_2O_5, 99.9%, −325 mesh, Sigma-Aldrich), molybdenum oxide (MoO_3, 99.9%, 6 μm, US Research

Table 1. Expected molar amount (%) in the final C-x samples. N is the number of added metals (Me), T_{MAX} is the peak temperature of the 2nd thermal cycle (TC) using the vacuum furnace carbolite GERO (G) or the SPS one.

		Molar amount % of added Me_i, $\sum_{i=1}^{N} Me_i = 100\%$								
		Example: C-1, $N = 4$, $(Hf_{0.25}Nb_{0.25}Ta_{0.25}Zr_{0.25})B_2$								2nd TC
C-x	N	Ti	Zr	Hf	Ta	Nb	Mo	W	Me′	Furnace-T_{MAX}
1	4	25	25	25	—	25	—	—	—	G—2373 K
2	4	25	25	—	25	—	25	—	—	G—2373 K
3	4	25	25	25	—	—	25	—	—	G—2373 K
4	5	20	20	20	—	20	20	—	—	G—2373 K
5	5	20	20	20	20	—	20	—	—	G—2373 K
6	5	21	21	21	—	—	21	16	—	G—2373 K
7	5	20	20	—	20	20	20	—	—	G—2373 K
8	5	23.75	23.75	23.75	23.75	5	—	—	—	SPS—2373 K
9	5	22.5	22.5	22.5	22.5	10	—	—	—	SPS—2373 K
10	5	21.25	21.25	21.25	21.25	15	—	—	—	SPS—2373 K
11	5	20	20	20	20	20	—	—	—	SPS—2373 K
12	5	20	20	20	20	—	—	—	20 Cr	SPS—2273 K
13	5	20	20	20	20	—	20	—	—	SPS—2273 K
14	5	20	20	20	20	—	—	20	—	SPS—2373 K
15	5	20	20	20	20	—	—	—	20 V	SPS—2373 K
16	5	21	21	21	—	21	—	16	—	G—2373 K
17	5	20	20	20	—	—	20	20	—	SPS—2373 K
18	6	17	17	17	—	17	17	15	—	G—2373 K
19	6	16.7	16.7	16.7	16.7	16.7	16.7	—	—	G—2373 K
20	6	16.8	16.8	16.8	16.8	—	16.8	16	—	G—2373 K
21	7	14.3	14.3	14.3	14.3	14.3	14.3	14.2	—	G—2373 K

Nanomaterials, Houston, TX), tungsten oxide (WO_3, 99.9%, ∼80 nm, Inframat Advanced Materials, Manchester, CT), vanadium oxide (V_2O_5, 99.6%, −10 mesh, Alfa Aesar, Tewksbury, MA), chromium oxide (Cr_2O_3, 99.5%, 0.7 μm, Elementis, Corpus Christi, TX). Purity and typical sizes are from the manufacturer datasheets. The expected final compositions of the C-x diborides, $x = 1$ to 21, are shown in table 1. The calculated combinations of Me oxides were weighted together with the reducing agents C and B_4C. C was added in stoichiometric quantity while B_4C was added in excess of about 13 wt% to the stoichiometric value to all batches to compensate for the loss of B during synthesis. Reference reactions and other details about the synthesis are reported in the supplementary information (SI) separate file. In brief, the synthesis consisted of two separate thermal cycles (TCs). The first was always carried out at 1923 K for 3 h in a vacuum furnace (Carbolite GERO LHTG 200–300/24 1G) whilst, for the second cycle of some C-x compositions, a spark plasma sintering (SPS) furnace (DCS10, Thermal Technology) was used to heat the powders already treated during the first TC and apply up to 50 MPa. The main processing condition differences between the compositions completely processed using the vacuum furnace or the SPS furnace were the extra applied pressure of 50 MPa and the faster heating/cooling rates for the latter method. The Carbolite GERO vacuum furnace was let to cool down from 2373 K naturally, implying a return to room temperature of several hours. Conversely, when the SPS furnace was used, the die-sample-piston assembly cooled to about 1273 K at 50 K min^{-1} and under a uniaxial pressure of 25 MPa and then cooled at the natural furnace rate to room temperature.

A field emission scanning electron microscopy (FESEM, ZEISS ∑igma—Germany) equipped with an energy dispersive spectroscopy (EDS) detector (INCA Energy 300, Oxford Instruments—UK) was used to characterize the compositions of the synthesized products. The heat-treated C-x pellets were pulverized for SR-XRPD acquisitions at room temperature and up to 1273 K. SR-XRPD data were collected at 17 keV ($\lambda = 0.7293$ Å) on the high-resolution MCX beamline at the Elettra synchrotron light-source (Trieste, Italy). The instrument profile was calculated using a Si standard (NIST SRM 640c) by refining the peaks shape with the pseudo-Voigt function available in the GSAS-II suite [21]. Quartz capillaries (0.2 or 0.3 mm diameter, depending on the sample absorption) were filled with powders and sealed under vacuum with a cutting torch. Diffraction patterns were acquired in Debye–Scherrer geometry on the 4-circle Huber goniometer while spinning the capillary at 300 rpm. SR-XRPD patterns were collected *in situ* at temperatures of 298, 573, 773, 873, 973, 1073, 1173, and 1273 K. The heating rates were 5–10 K min^{-1} and heat was supplied by a gas-blower (Oxford Danfysik DGB-0002). Patterns were collected after allowing a dwell time of 180 s for temperature stabilization. The gas-blower setup is specifically designed for this purpose, and uniform heating is achieved by fluxing a constant linear rate of hot air directly under the horizontally spinning capillary at a

fixed distance (4–5 mm). The heating profile for this setup is calibrated and it is constant over a lateral region of about 10 mm and vertical region of about 5–6 mm. Since the spinning capillary has an external diameter of 0.3 mm, and the sizes of the SR beam hitting the sample are 0.2 × 0.3 mm. It follows that (a) the probed volume of the capillary is well within the region of temperature stability and (b) the fraction of sample inside the capillary that is probed is at constant temperature. Thus, thermal gradients are expected to be negligible. In a few cases, SR-XRPD patterns were collected also during cooling, with isothermal holds at the temperatures of the selected intermediate steps. Data were then analysed by means of Rietveld method, and cell parameters refined for all temperatures, maintaining a reduced *R*-factor (R_{wp}) in the range of 6%–8%.

A dimensionless, Poisson-like, temperature dependent index (v) was calculated as

$$v\,(T) = \frac{\epsilon_{ab}}{\epsilon_c} \tag{1a}$$

with

$$\epsilon_{ab} = \frac{\sqrt{\left|a_T^2 - a_{298K}^2\right|}}{a_{298K}} \tag{1b}$$

$$\epsilon_c = \frac{\sqrt{\left|c_T^2 - c_{298K}^2\right|}}{c_{298K}} \tag{1c}$$

where a_T, c_T, a_{298K}, and c_{298K} are the experimental refined values for the cell parameters at various temperatures. ε_{ab} and ε_c are, respectively, the in-plane and out-of-plane relative lattice strains. Hereafter, the index $v\,(T)$ will be used to account for any excess in strain developed inside the lattice.

TE, when possible, was obtained as the relative variation of the cell parameters a_T and c_T with respect to the values a_{298K} and c_{298K}. According to the approach used by Lonnberg in [22] and by Dai *et al* in [15] the cell parameters a_T and c_T were fitted (in temperature) to a second order polynomial function

$$a_T = p_0 + p_1 T + p_2 T^2 \tag{2}$$

$$c_T = q_0 + q_1 T + q_2 T^2. \tag{3}$$

The temperature-dependent volume V_T of the hexagonal AlB_2-type lattice was calculated according to the following relation

$$V_T = \frac{\sqrt{3}}{2} a_T^2 c_T \tag{4}$$

using the refined cell parameters a_T and c_T. The average coefficients of TE (CTE) α_a and α_c, respectively along the *a*- and *c*-axis, were then derived using the fitted functions (2) and (3) for the cell parameters as

$$\alpha_a\,(T) = \frac{[a_T - a_{298K}]}{a_{298K}\,(\Delta T)} \tag{5}$$

$$\alpha_c\,(T) = \frac{[\,c_T - c_{298K}]}{c_{298K}\,(\Delta T)} \tag{6}$$

$$\alpha_{AV}\,(T) = \frac{(2\alpha_a + \alpha_c)}{3}. \tag{7}$$

With ΔT the difference from the temperature considered and room temperature (i.e. 298 K). Furthermore, the descriptor $\delta_{\Delta\chi}$, defined as

$$\delta_{\Delta X} = \sqrt{\sum_{i=1}^{N} y_i \left(1 - \frac{\Delta X_i}{\overline{\Delta X}}\right)^2},\ \overline{\Delta X} = \sum_{i=1}^{N} y_i \Delta X_i \tag{8}$$

was implemented to handle the varying chemical diversity due to the coexistence of *N* different metallic atoms with differing EN $\Delta\chi_i$, $\Delta\chi_i = \chi_{B} - \chi_{Me}$, for a certain molar concentration (y_i).

3. Results and discussion

The SR-XRPD patterns of all the C-*x* compositions collected at 298 K and relative Rietveld refinements are presented in figures (SI-1–SI-4). All patterns were indexed to a single-phase hexagonal lattice with P6/*mmm* symmetry, basically ruling out the presence of other residual secondary phases. A selection of FESEM micrographs imaged in the compositional mode (i.e. using the backscattered electron detector) is presented in figure 1 where only residual porosity is discernible as black spots. In figure 1, small regions highlighted by darker grey levels, and having a 'core-rim' structure, characterize the series of materials with an increasing content of Nb (i.e. C-8, C-9, C-10 and C-11). The presence of such features has already been observed 16, where they were identified as areas richer in Nb (compared to the surrounding volume). In the present case, there was no extra reflections attributable to such features in the SR-XRPD patterns, suggesting either an amount well below the threshold of detection for this technique (<1 wt%), or a marginal variation in the lattice parameters that would contribute to a slight increase in the microstrain broadening, not new for this class of materials. In fact, a recent article [23] confirmed the presence of Nb-rich areas, still invisible to a technique like SR-XRPD. For these reasons, an eventual influence of such areas on TE was considered negligible.

The random orientation of various grains in respect to the impinging electron beam direction leads to have an enhanced orientation contrast which causes changing grey levels of adjacent grains having the same chemical composition. The overall chemical compositions were assessed by EDS analysis of polished pieces of the as-synthesized samples. The compositions deviated from the expected values but were within range of ±2 at% (on metals basis). This means that the molar fractions listed in table 1 are representative of the studied systems.

SR-XRPD patterns acquired at regular temperature steps are presented in figure 2 for C-*x* composition with $x = 13$, 14, 15, and 19 to describe the general trends that were observed.

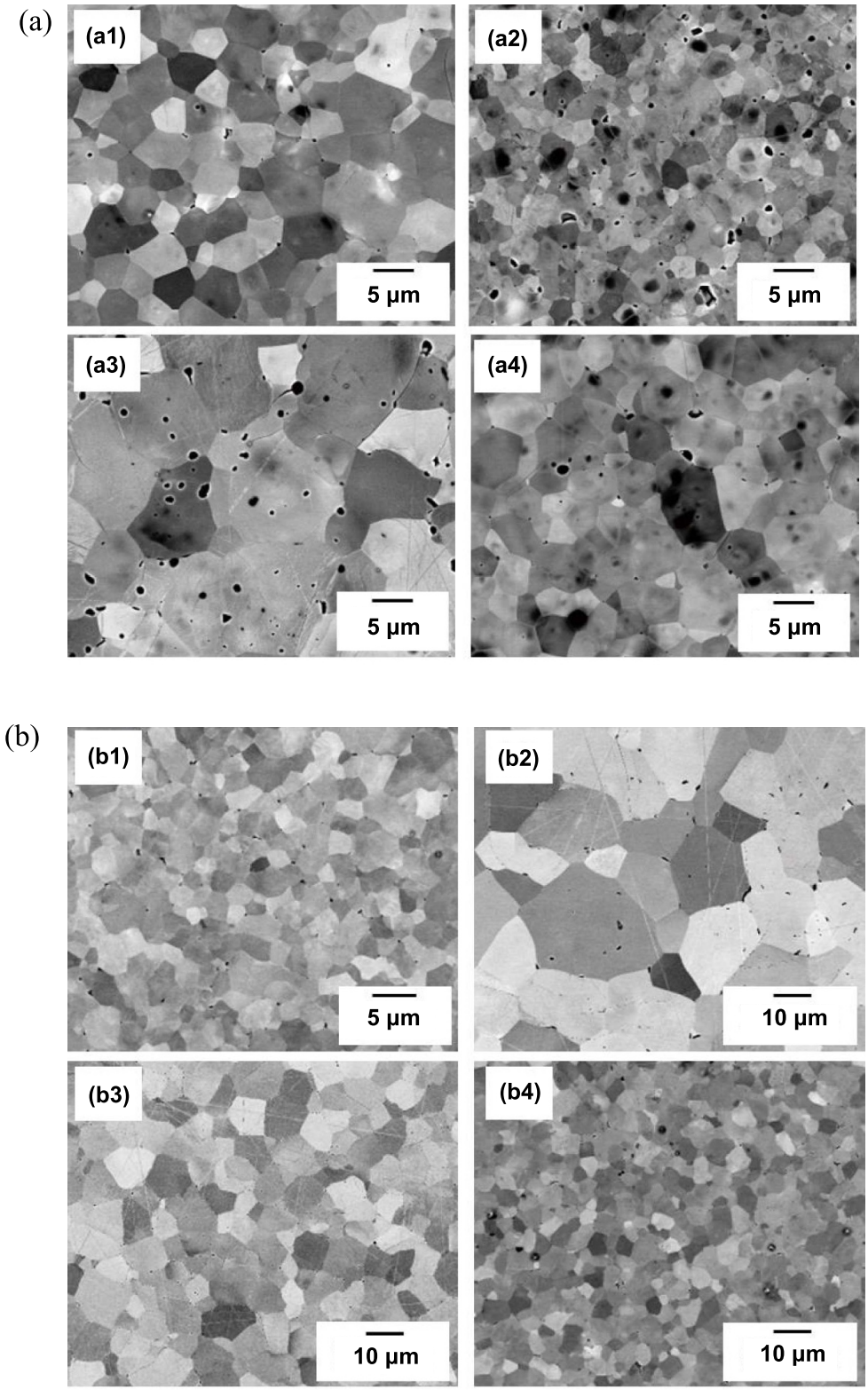

Figure 1. (a) Back-scattered mode—FESEM micrographs from C-8 (a1), C-9 (a2), C-10 (a3) and C-11 (a4). (b) Back-scattered mode—FESEM micrographs from C-12 (b1), C-13 (b2), C-14 (b3) and C-15 (b4).

The variable temperature SR-XRPD patterns showed little variation from those observed at room temperature, mostly slight changes in the lattice parameters, which are reported in figures 3–5.

The individual transition metal diborides have intrinsic anisotropy due to their hexagonal structure [22, 24]. The anisotropy was exacerbated due to the presence of multiple metals populating the same 1*a* Wyckoff site in the metal sub-lattice.

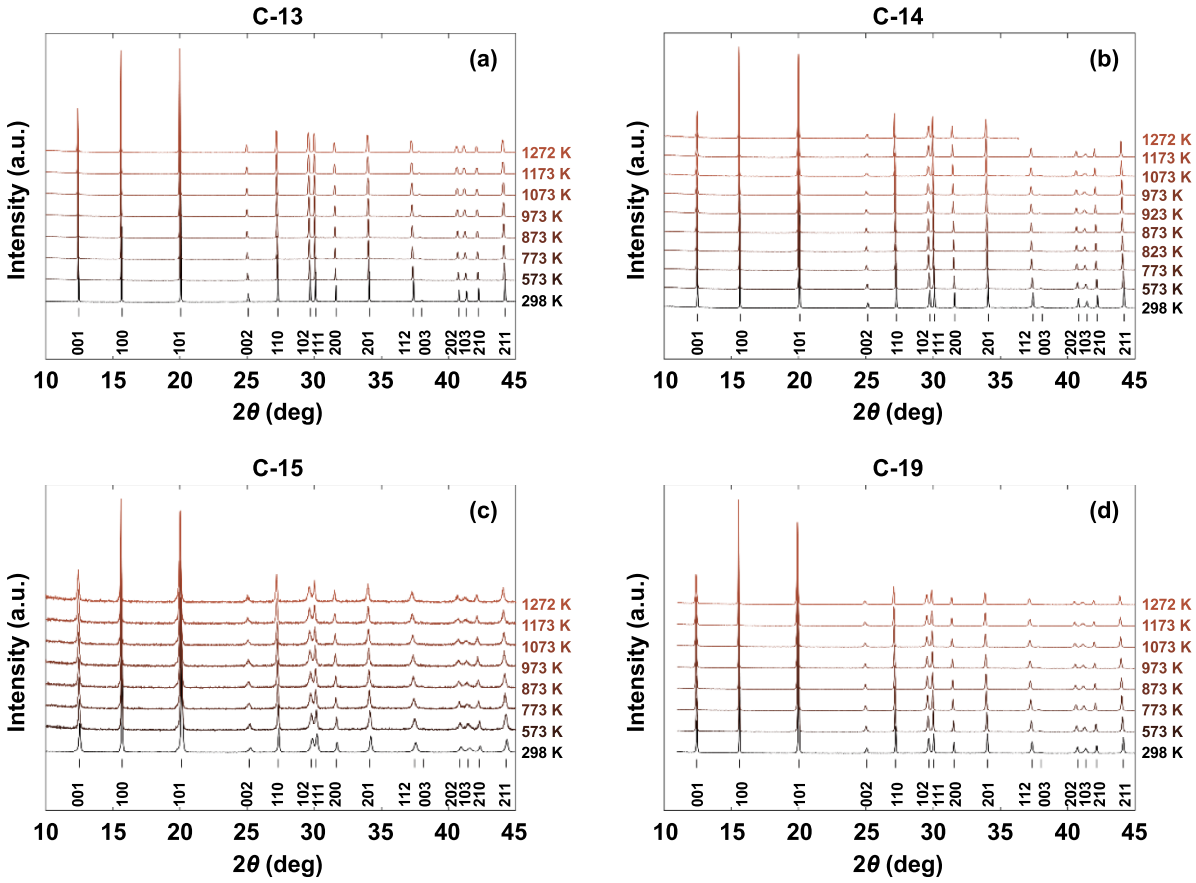

Figure 2. SR-XRPD patterns collected during the ramp of compositions C-13 (a), C-14 (b), C-15 (c), and C-19 (d).

The values of $v(T)$ were used to divide the compositions listed in table 1 into two subgroups, hereafter named G1 (for which $v(T) \leqslant 1$for all temperatures, cfr. figure 3) and G2 (for which $v(T) > 1$ see also figures 4 and 5).

This criterion, although arbitrary, matches with the deviation of the c-axis from a monotone increase observed for some compositions with increasing temperatures (cfr. figures 4 and 5) and for which the quadratic trend of equation (3) fails to fit the experimental data. More detailed information about index v and its trend are reported in the SI file.

The experimental values of a_{298K}, c_{298K}, and cell volume V_{298K}, as well as those calculated based on the RoM, are reported in tables SI-1 and SI-2. To calculate the RoM model, the source of the data for most of the single MeB_2 phases was taken from [22] while data for WB_2 came from [25].

To confirm a former experiment previously conducted on (Hf,Nb,Ta,Ti,Zr)B_2 (C-11 composition), the cell parameters measured in the present study changed with temperature in a way that cannot be predicted from the assumption of an ideal solid solution. In fact, the best fitted values of the second- and first-order polynomial parameters were only calculated for the group G-1 compositions (see table SI-3 and table 2). Our experimental data never matched linear rule of mixture prediction that would be expected if the compositions exhibited ideal solid solution behaviour. The temperature dependence of the c-axis lattice parameter deviated significantly from RoM predictions.

$$\alpha_a(T) = \alpha_{a,0} + \alpha_{a,1} T \tag{9}$$

$$\alpha_c(T) = \alpha_{c,0} + \alpha_{c,1} T \tag{10}$$

$$\alpha_{AV}(T) = \alpha_{AV,0} + \alpha_{AV,1} T \tag{11}$$

This is likely due to distortion of the Me-B bonds caused by the coexistence of different metals on the same 1a site. In contrast, the RoM model for the a-axis lattice parameter showed only a minor departure from the data. The variation in chemical complexity was related not only to an increasing number of metals populating the same degenerate site but also to their specific metal combination that led to emblematic cases where, for instance, the average TE α_{AV} exhibits a negative slope ($\alpha_{AV,1}$) as a function of temperature.

The average TEs of the DSSs deviated from the regular (monotonic) trend described by Lönnberg for the single-metal MeB_2 compounds [22], which could be due to either intrinsic and/or extrinsic factors. Extrinsic factors could be related to the processing conditions, i.e. the sequence of procedures

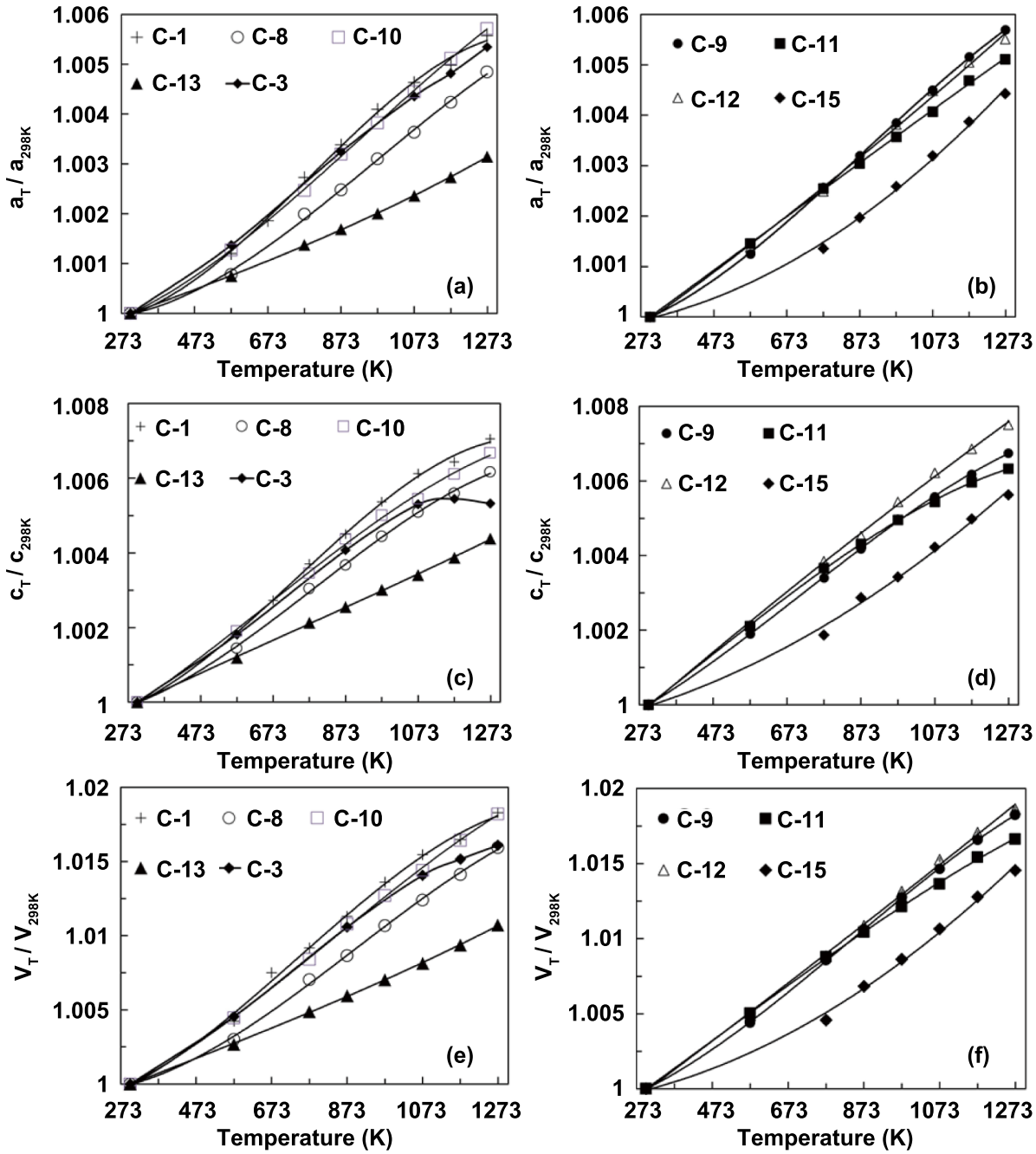

Figure 3. Group G1 of nine C-*x* compositions: solid lines are second-grade polynomial fits (see main text) to the experimental values of a_T/a_{298K}, c_T/c_{298K}, and V_T/V_{298K} versus temperature. Refined values of a_{298K}, c_{298K}, and V_{298K} are reported in table SI-1.

that lead the system to reach, or not, its maximum extent of long-range chemical homogeneity. In particular, grain orientation and micro cracking are common extrinsic effects observed in bulk ceramic materials. Both grain orientation and micro cracking produce highly non-linear trends in TE, including hysteresis, especially in anisotropic structures [26]. The group G2 samples are expected to exhibit extrinsic effects. On the other hand, even perfectly homogeneous HE materials should exhibit differences in attractive forces between the two sub-lattices that fluctuate locally from one type of metal to another, and which we consider to be an intrinsic effect. Larger (in radius size) and less electronegative atoms such as Zr or Hf have different Me–B bond-strengths than smaller and more electronegative metals such as Mo or W. In this regard, some metals will exert a compressive effect on the lattice (i.e. positive pressure) while others will produce local expansion (i.e. negative pressure). The sum of these 'chemical pressures' will be reflected in the average lattice parameters observed at room temperature. However, each type of metal can also exhibit different temperature-dependent trends.

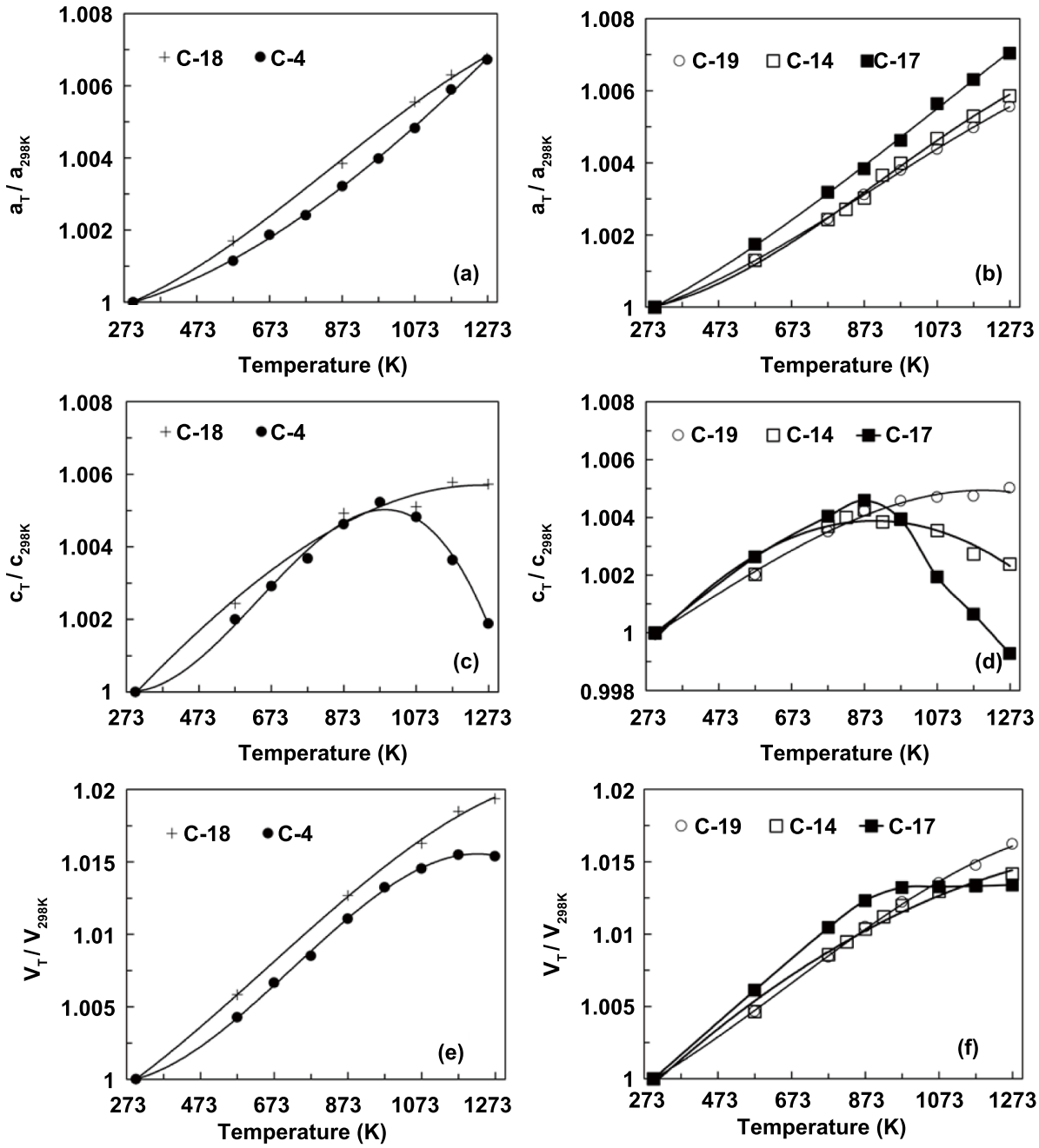

Figure 4. Group G2 (first part) of five C-*x* compositions: solid lines are a guide to the eye for the refined values of a_T/a_{298K}, c_T/c_{298K}, and V_T/V_{298K}. Refined values of a_{298K}, c_{298K}, and V_{298K} are reported in table SI-2.

While the behaviour could be similar at 298 K, differences may increase as temperature increases, which would affect the TE behaviour in the out-of-plane direction in some of the group G1 compositions (see figure 3).

The differences in EN $\Delta\chi_i = (\chi_{B} - \chi_{Me})$ between boron (i.e. the charge acceptor) and Me (i.e. the charge donor) and the dispersion in EN difference $\delta_{\Delta\chi}$ were calculated for every C-*x* composition. $\Delta\chi_i$ was thus used with a double purpose. The first was as a preliminary estimate of the degree of charge transfer keeping in mind that smaller values of $\Delta\chi_i$ imply mixtures of ionic, covalent, and metallic bonding, while larger values of $\Delta\chi_i$ surmise an increasing ionic character of the Me–B bonds. The second purpose was to correlate the different to the excess cell volume (EXV) calculated as

$$\mathrm{EXV} = \frac{\sqrt{\left|\left(V_{298K}^{RR}\right)^2 - \left(V_{298K}^{RoM}\right)^2\right|}}{V_{298K}^{RoM}} \qquad (12)$$

where V_{298K}^{RR} and V_{298K}^{RoM} are, respectively, the cell volume value obtained by Rietveld refinement and the by a RoM of an ideal solid solution. V_{298K}^{RR} and V_{298K}^{RoM} are reported in table SI-2: an increasing value of EXV is expected to be affected by an increasingly larger departure from a nearly

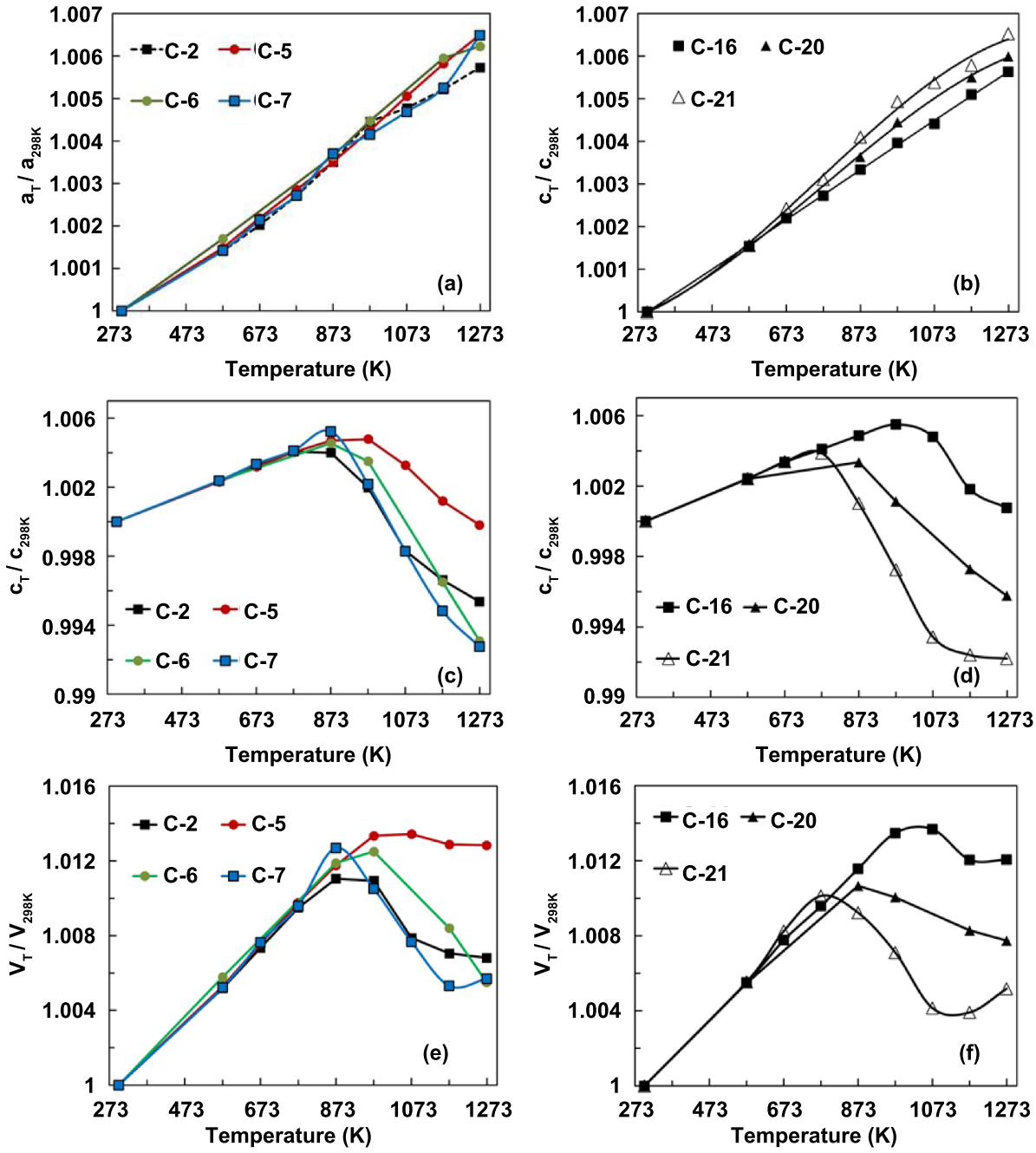

Figure 5. Group G2 (second part) of seven C-*x* compositions: solid lines are a guide to the eye for the refined values of a_T/a_{298K}, c_T/c_{298K}, and V_T/V_{298K}. Refined values of a_{298K}, c_{298K}, and V_{298K} are also reported in table SI-2.

ideal multi-element solid solution. The $\delta_{\Delta\chi}$ values calculated using equation (8) are plotted, respectively, against the weighted average of $\Delta\chi_i$ or EXV in figures 6 and 7. As for the $\delta_{\Delta\chi}$ versus EXV trend is concerned, it emerges that, *preferentially*, the C-*x* compositions grouped as G1 exhibited a reduced volume excess compared to compositions grouped as G2. Except in rare cases (i.e. C-12 and C-13), the group identity nicely matched, meaning that the lower values of $\delta_{\Delta\chi}$ preferentially pertain limited excess volume EXV. In other words, it is expected that more obvious deviations from ideality might take place when a certain cut-off is exceeded: based on the current reasoning a $\delta_{\Delta\chi}$ value of about 20% seems to delimit two domains. Composition C-3, C-12 and C-13 appear to escape this pattern. If C-3, due to its borderline group identity (see next discussion), can still be not considered an anomaly, for C-12 and C-13 a plausible explanation is under consideration. Composition C-13, although its $\delta_{\Delta\chi}$ is very close to the indicated cut-off, the corresponding excess volume EXV lies in the range typical of the group G2 compositions. Among the compositions grouped in G1, C-13 (as well as C-3) hosts a species like Mo: the reason of such a difference may arise from the uncertainty related to the tabulated cell parameters for the MoB_2 which is known to be a phase with a very difficult processability down to RT.

Table 2. G1 group of C-*x* compositions: best-fitted parameters of equations (8)–(10). Values of $\alpha_{a,0}$ as well as $\alpha_{c,0}$ and $\alpha_{AV,0}$ inform about the thermal expansion at room temperature.

	Equation (9)		Equation (10)		Equation (11)	
	$10^{-6}\ \alpha a_{,0}$ (K^{-1})	$10^{-10}\ \alpha_{a,1}$ (K^{-2})	$10^{-6}\ \alpha_{c,0}$ (K^{-1})	$10^{-10}\ \alpha_{c,1}$ (K^{-2})	$10^{-6}\ \alpha_{AV,0}$ (K^{-1})	$10^{-10}\ \alpha_{AV,1}$ (K^{-2})
C-1	5.87	1.09	8.91	−1.05	6.88	−2.79
C-3	5.67	−0.71	6.95	−1.03	6.13	−0.82
C-8	2.87	17.7	6.58	−0.31	4.1	11.7
C-9	4.82	9.4	8.0	−7.1	5.87	3.9
C-10	4.55	11.4	8.54	−12.5	5.9	3.4
C-11	5.38	−0.85	9.63	−23.8	6.8	−8.5
C-12	5.04	6.15	8.62	−6.2	6.23	2.0
C-13	2.27	7.3	4.33	1.1	3.0	5.2
C-15	0.83	30.2	2.33	28.3	1.34	29.6

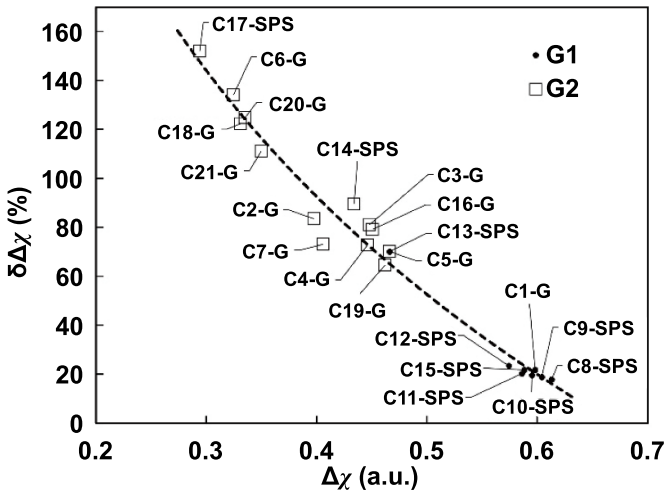

Figure 6. Dispersion of the difference in electronegativity ($\delta\Delta\chi$) versus the weighted average $\Delta\chi$ each C-*x* composition is displayed with a different symbol for groups G1 or G2 and labelled according to the processing history: G (GERO, without pressure) or SPS (with extra pressure).

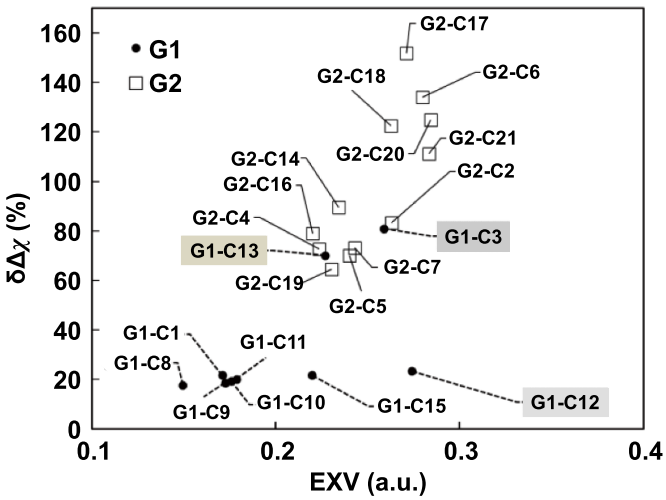

Figure 7. Dispersion of the difference in electronegativity ($\delta\Delta\chi$) versus the excess volume (EXV) calculated according to equation (8). Each C-*x* composition is displayed with a different symbol for groups G1 or G2 and labelled according to the processing history: G (GERO, without pressure) or SPS (with extra pressure).

The C-*x* compositions with larger $\delta_{\Delta\chi}$ values are expected to require more demanding synthesis conditions to achieve long-range chemical homogeneity. For example, compositions C-5 and C-13 (which have equivalent quantities of the same added metals) exhibited different TE behaviour when processed differently. A combination of a uniaxial pressure of 50 MPa and fast cooling rates (about 20 min from the target sintering temperature to 1273 K) promoted long-range chemical homogeneity. Conversely, the lack of uniaxial pressure together with slower cooling rates (e.g. several hours from the target sintering temperature to 1273 K) resulted in the formation of multiple phases, although the phases could not be distinguished from one to another by XRD in some cases. On the other hand, C-14 and C-17 were processed by SPS up to 2373 K, but did not appear to reach complete homogeneity, which is evident by examining deviation of the *c*-axis expansion behaviour as described by equation (3) and observed in figure 4. In the case of C-1, milder synthesis conditions were sufficient to reach the complete homogeneity.

For some of the compositions of group G1, the average coefficient of TE along the prismatic direction α_c decreased with increasing temperature in the range of 298–1273 K, which was tentatively ascribed to intrinsic effects. Composition C-3 was at the upper limit of homogenisability, with a borderline ν-index slightly within 1. The atomic distances increased systematically with temperature when a homogeneous solid solution formed (i.e. group G1). In this case, the range of tuneability of TE is wide, and TE can be engineered based on the combination of metals in the DSSs. The G2 compositions showed the highest non-linearity in TE and were termed non-regular. In the case of samples showing strong non-linearity and with ν index $\gg$1 (see figure SI-5 as example), the TE was influenced by extrinsic factors thus giving significant uncertainties in its determination.

The long-range chemical homogeneity of the solid solution, however complex it is, appears to be a pre-requisite for regular TE behaviour. The experimental data in table 2 of the G1 group samples, which showed a regular TE behaviour, were

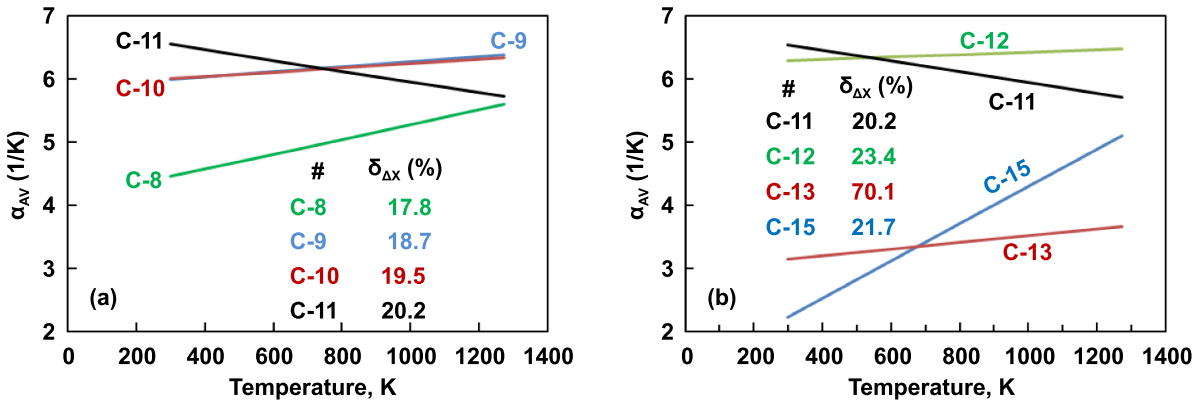

Figure 8. Average thermal expansion α_{AV} versus temperature of compositions aggregated in group G1-A (a) or G1-B (b): the corresponding $\delta_{\Delta\chi}$ values are indicated.

object of a systematic analysis, in the search of some RoM-inspired descriptors δ_Y capable of generating HEC design pipelines by capturing the correlations between the composition complexity and the mechanisms controlling the TE. One major challenge lies in fact in the prediction and understanding of the complex interplay between augmented configurational entropy ΔS_{MIX}, mixing enthalpy, cation size, coordination number and net exchanged charge transfer on the resulting functional properties such as the TE. The general descriptor δ_Y, already defined in the equation (8) for $Y = \Delta\chi_i$, has a native RoM-inferred rationale, and was used for other characteristics Y of the metals present: the atomic radius (R), the valence electron concentration (VEC), the EN, the atomic number (Z) and the atomic weight (MW). The descriptors δ_R, δ_{VEC}, δ_{EN}, δ_Z and δ_{MW} failed to provide an overall correlation between the two best-fitted parameters of equation (11) $\alpha_{AV,0}$ and $\alpha_{AV,1}$ for the group G1 compositions. This result confirms that RoM-inspired approaches can hardly elucidate the new functionalities induced by the coexistence of different species in the same sub-lattice. To give more elements of discussion by still granting credit to a RoM-inspired context the only descriptor $\delta_{\Delta\chi}$ provided interesting results for limited but homogeneous aggregates of samples: C-8/C-9/C-10/C/11 and C-11/C-12/C-13/C-15. In fact, it was important to find composition-structure-property interrelationships putting together $\alpha_{AV,0}$ and $\alpha_{AV,1}$: looking at equation (11) and table 2, more than $\alpha_{AV,0}$ the slope $\alpha_{AV,1}$ of the temperature changing curve of α_{AV} reflects the impact of the compositional heterogeneity on the TE functionality. The first aggregate was labelled G1-A and includes four compositions with the same five metals Ti–Zr–Ta–Hf–Nb, Nb varying from 5 to 20 at% (metal basis); the second aggregate was labelled G1-B and includes four compositions with Ti–Zr–Ta–Hf as base building block, and a fifth changing metal Nb, Cr, V or Mo. The C-14 composition, potential member of the G1-B aggregate, was excluded because it fell outside of the G1-group. Measurable effects of the compositional diversity on the TE behaviour were observed not only on $\alpha_{AV,0}$ (the average TE at room temperature) but also on $\alpha_{AV,1}$, i.e. amplitude and slope of the average TE variation versus temperature. The two aggregates are characterized by reverse opposite trends of $\alpha_{AV,0}$ against $\alpha_{AV,1}$ (see the equation (11) for the definition). If for the G1-A samples the increasing addition of Nb is the clearly identifiable feature controlling the inverse trend, for the compositions of the G1-B aggregate the characteristic feature remains much more elusive. Taking each aggregate as a separate subsystem, the weighted average difference in EN already plotted in figure 6 proved be pertinent to account for the observed opposite trends of α_{AV} at 298 K against $\alpha_{AV,1}$. Figure 8 is a graphical intuitive sketch which aims at displaying that, in the case of aggregate G1-A, the increase in $\delta_{\Delta\chi}$ due to the addition of Nb follows the inverse proportionality between α_{AV} at 298 K and $\alpha_{AV,1}$. The equivalent change of one only metal in the case of the samples falling inside the aggregate G1-B led to an inverse proportionality between α_{AV} at 298 K and $\alpha_{AV,1}$ but without fully respecting the order of an increasing $\delta_{\Delta\chi}$. It follows that not even the calculated difference in EN only based on a ROM model cannot fully account for the observed trends. In addition, the electronic structures of DSSs, and more in general of the compositionally complex HE ceramics, depends on the lattice distortion which leads to significant charge redistribution. The *in-situ* generated diverse nature of bonding further makes accurate prediction of the properties very challenging. The design and synthesis of single-phase ceramics appear better suited if combined to a bond-parameter guided strategy supported by machine-learning methodology or computational methods such as density functional theory (DFT) or montecarlo calculation and molecular dynamics (MC + MD) in order to manage, orient, and understand the compositional complexity of such HECs.

More in general, departures from homogeneity can be responsible for the largest variations from linearity observed along the *c*-axis in group G2 samples. The full-scale magnitude of ε_{ab} or ε_c (see figure SI-6) remains in the order of 10^{-1}%. The acquisition of data during cooling provided further insight. In figure 9, the cell volume V_T (defined in equation (4)) of samples C-5 and C-13 (made from the same starting composition but with different processing conditions) are compared during heating and cooling. Sample C-5, processed without applied pressure, exhibited hysteresis in the change in volume, which is attributed to the extrinsic effect of relaxation of strains accumulated during the first cooling.

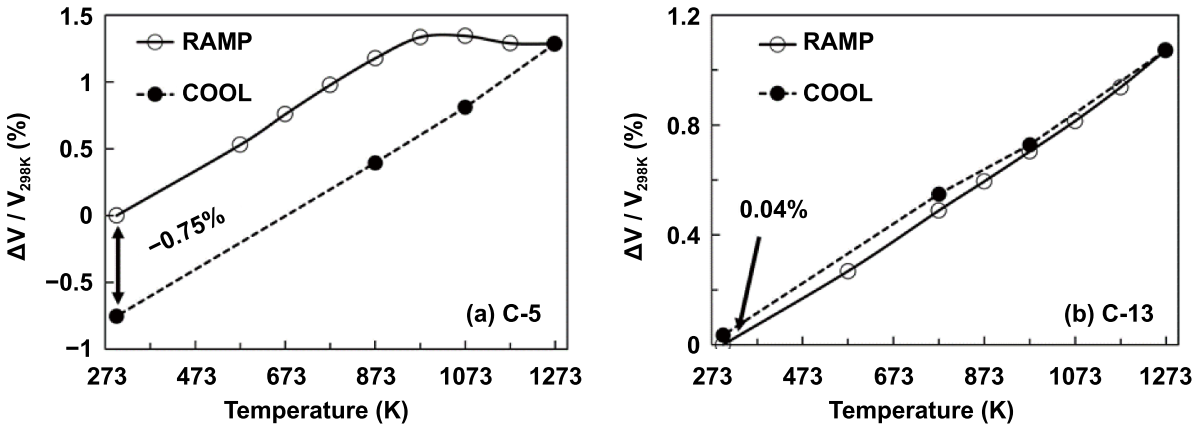

Figure 9. Relative change of the lattice volume $\Delta V/V_{298K}$, $\Delta V = (V_T\text{-}V_{298K})$, as a function of temperature during heating and cooling of sample C-5 and C-13: sign and magnitude of the residual volume difference are also indicated.

On the other hand, sample C-13 (synthesized with an applied mechanical pressure) did not show hysteresis with very low overall residual strain, suggesting its TE was controlled by an intrinsic behaviour.

The anisotropic character of TE in the class of diboride multi-element solid solutions was largely proven in the present work. Moreover, the different range of variability along the basal (i.e. α_a) or the prismatic direction (i.e. α_c) holds the interesting function to enable the TE tuneability versus temperature. Actually, the amplification of the TE anisotropy by playing through the difference between α_a and α_c can conceal an underestimation of uneven residual strains arising inside the material due to non-negligible anisotropy. The *in-situ* generated residual thermal strains can lead to micro-cracking, as recently reported by Monteverde *et al* [16] who studied a composition very similar to C-11. The target of α_c-to-α_a ratio values versus temperature close to unity should guide the design and fabrication of DSSs less vulnerable to the adverse effects of the occurrence of uneven residual strains.

4. Conclusions

A selection of 21 single-phase HE AlB_2-type DSSs was successfully manufactured via boro-carbothermal reduction of metal oxides followed by sintering at 2373 K. Their structure and thermal lattice expansion, far from ideal RoM based predictions, were studied *in-situ* using high-resolution synchrotron diffraction. Composition and processing conditions were pivotal in driving thermo-elastic trends and anisotropy. In particular, in-plane and out-of-plane non-linear TE were found to be strongly dependent not only on the chemical complexity and composition but also on the processing condition, with $(Hf,Ta,Ti,V,Zr)B_2$ and $(Hf,Nb,Ti,Zr)B_2$ solid solutions showing relatively the minimum (i.e. 1.3×10^{-6} K^{-1}) and maximum (i.e. 6.9×10^{-6} K^{-1}) values. At the same time, extrinsic effects on the TE were observed when the maximum extent of long-range homogeneity was not achieved. Overall, this work provides a guideline for scientists and engineers interested in the synthesis of this new class of compounds, drawing a simple relation between the average EN and chemical complexity connected to the best sintering process and suggesting a simple method to discriminate between intrinsic and extrinsic effects. Bond-parameter guided strategies supported by advanced computational methods are required to properly manage and understand the chemical complexity of such disordered systems.

Acknowledgments

We are grateful to Elettra-Sincrotrone Trieste for providing beamtime and financial support for the XRPD experiments (proposals nr. 20200101 and 20210215). The authors thank A Sangiorgi (ISSMC-CNR) for assistance in the high-temperature syntheses. The effort of L Feng, W Fahrenholtz and G Hilmas was supported by the U.S. National Science Foundation through Grant CMMI-1902069.

ORCID iD

Frédéric Monteverde https://orcid.org/0000-0002-9766-2275

References

[1] Cantor B 2021 Multicomponent high-entropy Cantor alloys *Prog. Mater. Sci.* **120** 100754
[2] Miracle D B and Senkov O N 2017 A critical review of high entropy alloys and related concepts *Acta Mater.* **122** 448–511
[3] Rost C M, Sachet E, Borman T, Moballegh A, Dickey E C, Hou D, Jones J L, Curtarolo S and Maria J P 2015 Entropy-stabilized oxides *Nat. Commun.* **6** 8485
[4] Zhang R Z and Reece M J 2019 Review of high entropy ceramics: design, synthesis, structure and properties *J. Mater. Chem.* A **7** 22148–62
[5] Feng L, Fahrenholtz W G and Brenner D W 2021 High-entropy ultra-high-temperature borides and carbides:

a new class of materials for extreme environments *Annu. Rev. Mater. Res.* **51** 165–85
[6] Yao Y, Yang F and Zhao X F 2022 Multicomponent high-entropy Zr-Y-Yb-Ta-Nb-O oxides for next-generation thermal barrier coating applications *J. Am. Ceram. Soc.* **105** 35–43
[7] Wright A J, Huang C Y, Walock M J, Ghoshal A, Murugan M and Luo J 2021 Sand corrosion, thermal expansion, and ablation of medium- and high-entropy compositionally complex fluorite oxides *J. Am. Ceram. Soc.* **104** 448–62
[8] Zhao Z F, Chen H, Xiang H M, Dai F Z, Wang X H, Xu W, Sun K, Peng Z J and Zhou Y C 2020 High-entropy $(Y_{0.2}Nd_{0.2}Sm_{0.2}Eu_{0.2}Er_{0.2})AlO_3$: a promising thermal/environmental barrier material for oxide/oxide composites *J. Mater. Sci. Technol.* **47** 45–51
[9] Zhou L, Li F, Liu J X, Hu Q, Bao W C, Wu Y, Cao X Q, Xu F F and Zhang G J 2020 High-entropy thermal barrier coating of rare-earth zirconate: a case study on $(La_{0.2}Nd_{0.2}Sm_{0.2}Eu_{0.2}Gd_{0.2})_2Zr_2O_7$ prepared by atmospheric plasma spraying *J. Eur. Ceram. Soc.* **40** 5731–9
[10] Zhao Z F, Xiang H M, Chen H, Dai F Z, Wang X H, Peng Z J and Zhou Y C 2020 High-entropy $(Nd_{0.2}Sm_{0.2}Eu_{0.2}Y_{0.2}Yb_{0.2})_4Al_2O_9$ with good high temperature stability, low thermal conductivity, and anisotropic thermal expansivity *J. Adv. Ceram.* **9** 595–605
[11] Xu L, Su L, Wang H J, Gao H F, Lu D, Peng K, Niu M and Cai Z X 2022 Tuning stoichiometry of high-entropy oxides for tailorable thermal expansion coefficients and low thermal conductivity *J. Am. Ceram. Soc.* **105** 1548–57
[12] Chen H, Xiang H M, Dai F Z, Liu J C and Zhou Y C 2020 High entropy $(Yb_{0.25}Y_{0.25}Lu_{0.25}Er_{0.25})_2SiO_5$ with strong anisotropy in thermal expansion *J. Mater. Sci. Technol.* **36** 134–9
[13] Xu L, Wang H J, Su L, Lu D, Peng K and Gao H F 2021 A new class of high-entropy fluorite oxides with tunable expansion coefficients, low thermal conductivity and exceptional sintering resistance *J. Eur. Ceram. Soc.* **41** 6670–6
[14] Iwan S, Burrage K C, Storr B C, Catledge S A, Vohra Y K, Hrubiak R and Velisavljevic N 2021 High-pressure high-temperature synthesis and thermal equation of state of high-entropy transition metal boride *AIP Adv.* **11** 035107
[15] Dai F Z, Sun Y J, Wen B, Xiang H M and Zhou Y C 2021 Temperature dependent thermal and elastic properties of high entropy $(Ti_{0.2}Zr_{0.2}Hf_{0.2}Nb_{0.2}Ta_{0.2})B_2$: molecular dynamics simulation by deep learning potential *J. Mater. Sci. Technol.* **72** 8–15
[16] Monteverde F, Saraga F, Gaboardi M and Plaisier J R 2021 Compositional pathways and anisotropic thermal expansion of high-entropy transition metal diborides *J. Eur. Ceram. Soc.* **41** 6255–66
[17] Feltrin A C, Hedman D and Akhtar F 2021 Transformation of metastable dual-phase $(Ti_{0.25}V_{0.25}Zr_{0.25}Hf_{0.25})B_2$ to stable high-entropy single-phase boride by thermal annealing *Appl. Phys. Lett.* **119** 161905
[18] Ge H J, Cui C F, Song H Q and Tian F Y 2021 Local lattice distortion in high-entropy carbide ceramics *Metals* **11** 1399
[19] Sangiovanni D G, Tasnádi F, Harrington T, Odén M, Vecchio K S and Abrikosov I A 2021 Temperature-dependent elastic properties of binary and multicomponent *high-entropy* refractory carbides *Mater. Des.* **204** 109634
[20] Zhang P X, Ye L, Chen F H, Han W J, Wu Y H and Zhao T 2022 Stability, mechanical, and thermodynamic behaviors of (TiZrHfTaM)C (M = Nb, Mo, W, V, Cr) high-entropy carbide ceramics *J. Alloys Compd.* **903** 163868
[21] Toby B H and Von Dreele R B 2013 *GSAS-II* : the genesis of a modern open-source all purpose crystallography software package *J. Appl. Crystallogr.* **46** 544–9
[22] Lönnberg B 1988 Thermal expansion studies on the group IV-VII transition metal diborides *J. Less-Common Met.* **141** 145–56
[23] Monteverde F, Saraga F, Gaboardi M, Feng L, Hilmas G and Fahrenholtz W 2022 Quantitative inspection of grain-scale chemical inhomogeneities in high-entropy AlB_2-type transition metal diborides *J. Am. Ceram. Soc.* **105** 6910–23
[24] Magnuson M, Hultman L and Högberg H 2022 Review of transition-metal diboride thin films *Vacuum* **196** 110567
[25] Jiang C L, Pei Z L, Liu Y M, Lei H, Gong J and Sun C 2014 Determination of the thermal properties of AlB_2-type WB_2 *Appl. Surf. Sci.* **288** 324–30
[26] Chu C N, Saka N and Suh N P 1987 Negative thermal expansion ceramics: a review *Mater. Sci. Eng.* **95** 303–8